



Transient simulation of a two-phase loop thermosyphon with a model out of thermodynamic equilibrium



S. Bodjona^{a,*}, E. Videcoq^a, R. Saurel^{b,c}, A. Chinnayya^a, A.M. Benselama^a, Y. Bertin^a

^a Institut Pprime CNRS-ENSMA-Université de Poitiers, Département Fluides, Thermique, Combustion, ENSMA Téléport 2, 1, avenue Clément Ader, BP 40109, F86961 Futuroscope Chasseneuil Cedex, France

^b Université Aix-Marseille, CNRS, Centrale Marseille, M2P2 UMR7340, 38 rue Joliot-Curie, 13451 Marseille, France

^c RS2N, 371 chemin de gaumin, 83640 Saint Zacharie, France

ARTICLE INFO

Article history:

Received 18 May 2016

Received in revised form 9 January 2017

Accepted 16 January 2017

Keywords:

Two-phase loop thermosyphon

Two-phase flows model

Goodwin equations of state

Stiffened Gas equation of state

HLLC

ABSTRACT

Numerical investigation of two-phase loop thermosyphon (2PLT) in steady and transient states is addressed. A one-dimensional two-phase flow model describing a liquid-gas mixture in both mechanical and thermal equilibrium but out of thermodynamic equilibrium is developed. The model considers subcooled liquid and over heated vapor as well as phase transition (evaporation and condensation). The flow model is solved with a specific hyperbolic solver based on Godunov method and Harten-Lax-van Leer-Contact (HLLC) Riemann solver. A parametric study on the thermal power at the evaporator is performed in steady and transient states, the aim being to determine the effects of thermal power increase at the evaporator on the loop behavior. The comparison between Goodwin and Stiffened Gas (SG) equation of state (EOS) models shows fair agreement for latent heat of vaporization, specific volume and enthalpy for both liquid and vapor phases. Simulation of four test cases, corresponding to different evaporator thermal loads, is also carried out in transient state showing that loop response is correctly reproduced by this numerical approach, novel in the context of thermosyphon loops.

© 2017 Elsevier Ltd. All rights reserved.

1. Introduction

A two-phase loop thermosyphon (2PLT) is a passive thermal system, often used for energy transportation. It contains coexisting liquid and vapor phases of a working fluid and consists mainly of an evaporator, a condenser, a liquid line and a vapor line. The evaporator is the locus of heat supplied to the working fluid while conversely the condenser is the location where heat extraction takes place. The vapor line connects the evaporator outlet to the condenser inlet, whereas the liquid line connects the condenser outlet to the evaporator inlet. Due to the high density power it can manage and its low thermal resistance, 2PLT has been found to be the most efficient device in several applications such as thermal stabilization [1], passive cooling system of the seat electronic box on commercial aircrafts board [2], telecommunication equipment in the outdoor cabinet [3], solar water heater [4,5], prevention of icing on a buoy [6], nuclear reactors with natural circulation [7–9] and geothermal energy [10,11].

Our interest in this work addresses the modeling of such a system in steady and transient states. In this area various

contributions have already been done. Vincent et al. [12] present a numerical model which is developed for a two-phase co-current thermosyphon. They use control volume approach and their investigation focuses on transient behavior of the system in the vicinity of steady-state conditions. They conclude that the approach of control volume limits the number of variables and describes satisfactorily the behavior of thermosyphons. Some of their results are confirmed by the experiment of Leidenfrost and Modrei [13]. Moreover, they note that the predictive ability of their model may be improved by accurate representation of the two-phase flow at the evaporator and the condenser. This control volume approach is also used by Dobran [14] and Reed [15] in their analytical investigation. A numerical model which takes into account the effects of riser diameter and its inclination angle in 2PLT solar water heater is presented by Nay Zar Aung et al. [16], intending to optimize the design of these loops. Yilmaz [17] also presents a numerical modeling of two-phase solar water heater which takes into account variable properties of the fluid with temperature, heat transfer in the collector and condenser and nonhomogeneous two-phase flow. As for the working fluid, he used refrigerants R12, R114, R11 and R113 and water. Only the results for refrigerant R11 are presented in his investigation. He showed that homogeneous flow model is not sufficient to describe the

* Corresponding author.

E-mail address: serge-heziewe.bodjona@ensma.fr (S. Bodjona).

Nomenclature

Greek symbols

α	volume fraction
γ	ratio of specific heat capacity at constant volume and pressure
Δt	time step, s
Δx	cell size, m
μ	dynamic viscosity of the fluid, $\text{kg}\cdot\text{m}^{-1}\cdot\text{s}^{-1}$
ρ	density, $\text{kg}\cdot\text{m}^{-3}$
Ω	volume, m^3

Roman symbols

A_{ext}	condenser exchange surface, m^2
c	sound speed, $\text{m}\cdot\text{s}^{-1}$
C_p	specific heat capacity at constant pressure, $\text{J}\cdot\text{kg}^{-1}\cdot\text{K}^{-1}$
C_v	specific heat capacity at constant volume, $\text{J}\cdot\text{kg}^{-1}\cdot\text{K}^{-1}$
D_h	hydraulic diameter, m
e	specific internal energy, $\text{J}\cdot\text{kg}^{-1}$
E	specific total energy, $\text{J}\cdot\text{kg}^{-1}$
F'	vector of local flux
$F_{i+\frac{1}{2}}, F_{i-\frac{1}{2}}$	numerical flux vector
G	Gibbs specific free energy, $\text{J}\cdot\text{kg}^{-1}$
g	gravity, $\text{m}\cdot\text{s}^{-2}$
h	specific enthalpy, $\text{J}\cdot\text{kg}^{-1}$
L	loop length, m
L_v	specific latent heat of vaporization, $\text{J}\cdot\text{kg}^{-1}$
\dot{m}	phase change rate per volume unit, $\text{kg}\cdot\text{m}^{-3}\cdot\text{s}^{-1}$
p	pressure, Pa
p_∞	pressure-like parameter, Pa
q	specific mixture reference energy, $\text{J}\cdot\text{kg}^{-1}$
Q	power, W
\dot{Q}_{cond}	power at the condenser, W

\dot{Q}_{evap}	power at the evaporator, W
q'	characteristic constant, $\text{J}\cdot\text{kg}^{-1}$
s	specific entropy, $\text{J}\cdot\text{kg}^{-1}\cdot\text{K}^{-1}$
S	vector of averaged source terms
S'	vector of source terms
S_L	expansion wave speed, $\text{m}\cdot\text{s}^{-1}$
S_M	contact wave speed, $\text{m}\cdot\text{s}^{-1}$
S_R	shock wave speed, $\text{m}\cdot\text{s}^{-1}$
T	temperature, K
t	time, s
U	vector of averaged conservative variables
u	velocity, $\text{m}\cdot\text{s}^{-1}$
U'	vector of local conservative variables
U^*	variable
v	specific volume, $\text{m}^3\cdot\text{kg}^{-1}$
x	curvilinear abscissa, m
y	vapor mass fraction

Subscripts

0; 1; 2; 3	reference thermodynamic state
<i>cold</i>	condenser ambient cold state
<i>cond</i>	condenser
<i>evap</i>	evaporator
<i>ext</i>	exterior
<i>g</i>	vapor
<i>Gd</i>	Goodwin
<i>k</i>	liquid and vapor generic index
<i>L</i>	left state
<i>l</i>	liquid
<i>R</i>	right state
<i>sat</i>	saturated thermodynamic state

two phase flow in the collector and that an optimum collector pipe diameter exists. Bielinski et al. [18] proposed a detailed analysis of heat transfer and fluid flow in a new generalized model of loop thermosyphon and its different variants. They showed that a one-dimensional two-phase separate flow model can accurately describe heat transfer and fluid flow in a 2PLT. Two different models for the evaporator and the condenser were used by Qu [19]. A bubble flow model is used at the evaporator and a Nusselt-liquid-film-like model is used at the condenser. One of the conclusions resulting of these investigations is that density of the vapor-liquid mixture at the evaporator outlet is not that of the vapor. He also observed that vapor velocity is three orders of magnitude higher than that of the liquid so that the liquid velocity can be neglected. Eduardo et al. [20] presented a one-dimensional loop model which is extended to variable area and steady state. They report the existence of multiple solutions, some of them being unstable.

In the works cited above in connection with the 2PLT, heat transfer, fluid flow and the behavior of the loop in transient and steady states have been studied in different ways. These one-dimensional models include mass, momentum and energy balances, each one having its own specification. Bielinski et al. [18] use incompressible flow model with Boussinesq approximation and empirical correlation in different parts of the loop. They also consider thermal equilibrium at all points of the loop. Steady and incompressible equations on the whole loop with Boussinesq approximation is also used by Ramos et al. [20]. Others authors such as Qu [19] or Vincent et al. [12] use different models for the evaporator, the condenser, the liquid line and the vapor line. Here each part of the loop has its own model, based either on hydraulic flow model or compressible flow model.

In the present study a one-dimensional flow model (Euler equations), considering a two phase mixture in both mechanical and thermal equilibrium is considered. In each part of the loop, the very same model is used in the computation. It can describe thermodynamic equilibrium (saturation or mixture), but also thermodynamic non-equilibrium (pure liquid or pure vapor) phase and so it can be used to compute phase transitions (liquid-mixture-vapor) straightforwardly. In order to represent accurately the possible wave fluctuations in the system, compressibility and wave propagation are considered.

The two-phase flow model used in this paper has been developed to model a wide spectrum of two-phase flow applications, such as cavitating, boiling, evaporating flows [21], nozzle flows of liquid-gas mixture [22]. To our best knowledge, the use of this kind of model for 2PLT is carried out here for the first time.

The paper is structured as follows: the 2PLT and its principles are briefly described in Section 2. The model of this system and the solution methodology are presented in Sections 3 and 4 respectively. Section 5 is devoted to discussion and analysis of four test cases, corresponding to different thermal loads applied on the evaporator.

2. Two-phase loop thermosyphon

As shown in Fig. 1, the 2PLT is a passive thermal system, mainly composed of an evaporator, a vapor line, a condenser and a liquid line. Its operation lies on the phase change of a working fluid (methanol in our case) and on gravity, which is the driving force of the fluid flow. At the evaporator (B-C), the methanol liquid phase is heated and vaporized. The vapor flows through the vapor line (C-

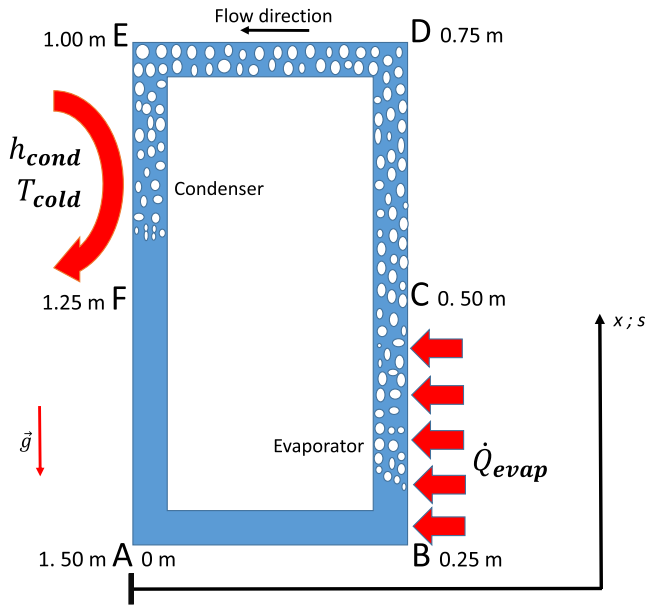


Fig. 1. Schematic representation of a 2PLT.

E) toward the condenser which consists in a low temperature controlled heat exchanger (E-F). The vapor is cooled and turns into liquid in the condenser. The liquid falls under gravity effect in the vertical liquid line (F-A) and is driven toward the evaporator by the horizontal liquid line (A-B) where it is heated again. If x is the curvilinear coordinate along the loop, g is the gravity, ρ is the mixture density and ϵ depends on gravity direction, see Fig. 1,

$$\epsilon = \begin{cases} -1 & \text{if } x \in [B, D] \\ 0 & \text{if } x \in [A, B] \cup [D, E], \\ 1 & \text{if } x \in [E, A] \end{cases} \quad (1)$$

then the integral $\int \epsilon \rho g dx$ is not zero because the density of the working fluid is higher in the descending section (E-A) than in the ascending section (B-D) in average. This effect is responsible of fluid circulation in the loop.

3. Flow model

3.1. Hypothesis

Basic assumptions of the flow model are:

- The tube cross-section area is constant along the loop.
- The two-phase flow is considered as a homogeneous mixture in both mechanical and thermal equilibrium; at a given location both phases share the same velocity, pressure and temperature.
- The fluid mixture is compressible, which allows the vapor density changing in the loop with space and time in order to satisfy balances and the equation of state.
- Friction effects are approximated by Darcy-Weisbach law.
- Heat conduction inside the fluid is neglected.
- The heat exchange coefficient h_{cond} is constant at the condenser.
- Except at the evaporator and the condenser, heat exchange with the environment is neglected.

3.2. Flow model

A homogeneous compressible flow mixture is considered [22]. This model is derived from a multiphase model of phase transition

considering wave's dynamics [23]. The assumptions listed in the previous section yield the following set of equations

$$\frac{\partial \rho}{\partial t} + \frac{\partial}{\partial x}(\rho u) = 0 \quad (2a)$$

$$\frac{\partial(\rho u)}{\partial t} + \frac{\partial}{\partial x}(\rho u^2 + p) = -\frac{64\mu}{2D_h^2} u + \epsilon \rho g \quad (2b)$$

$$\frac{\partial(\rho E)}{\partial t} + \frac{\partial}{\partial x}((\rho E + p)u) = \frac{\dot{Q}}{\Omega} + \epsilon \rho g u \quad (2c)$$

$$\frac{\partial(\rho y)}{\partial t} + \frac{\partial(\rho y u)}{\partial x} = \dot{m} \quad (2d)$$

where u , p , E and y are the velocity, pressure, total energy and vapor mass fraction respectively, \dot{m} is the evaporation/condensation rate per volume unit, Ω and D_h correspond to the volume and the hydraulic diameter, respectively. The thermal load \dot{Q} is defined by

$$\dot{Q} = \begin{cases} \dot{Q}_{evap} & \text{if } x \in [B, C] \\ 0 & \text{if } x \in [A, B] \cup [C, E] \cup [F, A], \\ \dot{Q}_{cond} = h_{cond} A_{ext} (T_{cold} - T) & \text{if } x \in [E, F] \end{cases} \quad (3)$$

where \dot{Q}_{evap} and \dot{Q}_{cond} are the thermal load at the evaporator and at the condenser, respectively. h_{cond} , A_{ext} , T_{cold} and T are the heat exchange coefficient, the exchange surface at the condenser, the cold (ambient) temperature and the working fluid mixture temperature, respectively. The viscosity μ appearing in the momentum balance of system (2), is the mixture viscosity given by Cicchitti et al. [24],

$$\mu = y\mu_g + (1 - y)\mu_l, \quad (4)$$

where μ_g and μ_l are the temperature-dependent vapor and liquid dynamic viscosity, respectively given by [25]

$$\mu_g = 3.0663 \times 10^{-7} \frac{T^{0.69655}}{1 + 205/T}, \quad (5)$$

$$\mu_l = \exp(-25.317 + \frac{1789.2}{T} + 2.069 \times \log(T)) \quad (6)$$

valid in the range 273.15–433.15 K.

Closure of System (2) requires the equation of state (EOS) to be specified. The mixture EOS can be expressed as

$$f(p, \rho, e, y) = 0. \quad (7)$$

Such EOS is derived from pure phases EOS, as detailed hereafter.

3.3. Equation of state for the pure phases

The two-phase flow model (2) requires the EOS for each pure phase and for the mixture to be given. Goodwin EOS [26] for each pure phase can be used to determine the mixture EOS. Let us recall that: (i) Goodwin EOS are correlations deduced from methanol pressure-density-temperature data in the range 176–673 K and up to 700 Bar, (ii) they apply only at thermodynamic equilibrium. Unfortunately, this implies loss of hyperbolicity in the mixture (or spinodal) zone [27]. This loss of the hyperbolicity of the model is characterized by imaginary sound speed ($c^2 = -v^2 (\frac{\partial p}{\partial v})_s < 0$) in the spinodal zone.

The work developed herein considers EOS of each phase in a way that each phase has its own thermodynamics, especially its own entropy (in such a way that $c^2 = -v^2 (\frac{\partial p}{\partial v})_s > 0$). This is done using “Stiffened Gas” (SG) EOS.

Another problem is highlighted by numerical computations. Indeed we use finite volume method coupled with the approximate Riemann solver called Harten-Lax-van Leer Contact (HLLC)

numerical scheme. The procedure of the HLLC scheme needs sound speed computation. Calculating the sound speed ($c^2 = -v^2 \left(\frac{\partial p}{\partial v}\right)_s$ or $c^2 = \frac{p + \left(\frac{\partial p}{\partial y}\right)_{p,y}}{\left(\frac{\partial p}{\partial v}\right)_{p,y}}$) requires the internal energy of each phase to be a function of p , ρ and y . Using Goodwin EOS and associated internal energy tables for each phase results in computational issues and excessive CPU cost. This issue is circumvented using SG EOS.

As presented by Le Metayer et al. [27], each phase is assumed to obey the SG EOS. That is the simplest complete thermodynamic formulation able to consider at the same time condensed matter and gases. It is a generalization of the ideal gas EOS where attractive molecular effects are considered in addition to elastic-choc molecular interaction. For each phase k , the SG EOS reads [27]

$$v_k(p, T) = \frac{(\gamma_k - 1)C_{v,k}T}{p + p_{\infty,k}}, \quad (8)$$

$$\rho_k(p, T) = \frac{1}{v_k(p, T)} = \frac{p + p_{\infty,k}}{(\gamma_k - 1)C_{v,k}T}, \quad (9)$$

$$e_k(p, T) = \frac{p + \gamma_k p_{\infty,k}}{\gamma_k - 1} v_k(p, T) + q_k, \quad (10)$$

$$h_k(p, T) = \gamma_k C_{v,k}T + q_k, \quad (11)$$

$$G_k(p, T) = h_k - Ts_k = (\gamma_k C_{v,k} - q'_k)T - C_{v,k}T \log\left(\frac{T^{\gamma_k}}{(p + p_{\infty,k})^{\gamma_k - 1}}\right) + q_k, \quad (12)$$

where G is the Gibbs free energy and v and h are the specific volume and the specific enthalpy, respectively. k denotes the phase (liquid, gas) and $C_{p,k}$, q_k , q'_k , $p_{\infty,k}$, $C_{v,k}$ and γ_k are constants to be computed from four reference points $(T_0, p_{sat}(T_0))$, $(T_1, p_{sat}(T_1))$, $(T_2, p_{sat}(T_2))$ and $(T_3, p_{sat}(T_3))$ on the liquid-gas saturation curves $p_{sat}(T)$. The fluid considered in the present work is methanol and the associated thermodynamic data are given in [26]. In particular saturation curves are available. The various constants are obtained from the following set of relations based on four reference points

$$C_{p,k} = \frac{h_{k,Gd}(T_1) - h_{k,Gd}(T_0)}{T_1 - T_0}, \quad (13)$$

$$q_k = h_{k,Gd}(T_0) - C_{p,k}T_0, \quad (14)$$

$$p_{\infty,l} = \frac{v_{l,Gd}(T_2)T_3 p_{sat,Gd}(T_2) - v_{l,Gd}(T_3)T_2 p_{sat,Gd}(T_3)}{v_{l,Gd}(T_3)T_2 - v_{l,Gd}(T_2)T_3}, \quad (15)$$

$$p_{\infty,g} = \frac{v_{g,Gd}(T_0)T_1 p_{sat,Gd}(T_0) - v_{g,Gd}(T_1)T_0 p_{sat,Gd}(T_1)}{v_{g,Gd}(T_1)T_0 - v_{g,Gd}(T_0)T_1}, \quad (16)$$

$$C_{v,l} = C_{p,l} - \frac{v_{l,Gd}(T_2)}{T_2} (p_{sat,Gd}(T_2) + p_{\infty,l}), \quad (17)$$

$$\gamma_k = \frac{C_{p,k}}{C_{v,k}}, \quad (18)$$

$$C_{v,g} = C_{p,g} - \frac{v_{g,Gd}(T_0)}{T_0} (p_{sat,Gd}(T_0) + p_{\infty,g}) \quad (19)$$

where subscripts l and g denote liquid phase and vapor phase, respectively.

In order to compute these constants in our study, we use four pairs: $(T_0, p_{sat}(T_0)) = (273 \text{ K}, 4 \times 10^3 \text{ Pa})$, $(T_1, p_{sat}(T_1)) = (332 \text{ K}, 8.1 \times 10^4 \text{ Pa})$, $(T_2, p_{sat}(T_2)) = (400 \text{ K}, 7.7 \times 10^5 \text{ Pa})$ and

$(T_3, p_{sat}(T_3)) = (482 \text{ K}, 4.743 \times 10^6 \text{ Pa})$. The value of the constants for both pure liquid and gas phases are summarized below:

$$\begin{aligned} C_{p,l} &= 2.815 \times 10^3 \text{ J}\cdot\text{kg}^{-1}\cdot\text{K}^{-1}, C_{p,g} = 7.772 \times 10^2 \text{ J}\cdot\text{kg}^{-1}\cdot\text{K}^{-1}, \\ C_{v,l} &= 1.363 \times 10^3 \text{ J}\cdot\text{kg}^{-1}\cdot\text{K}^{-1}, C_{v,g} = 5.226 \times 10^2 \text{ J}\cdot\text{kg}^{-1}\cdot\text{K}^{-1}, \\ \gamma_l &= 2.065, \gamma_g = 1.487, \\ p_{\infty,l} &= 3.635 \times 10^8 \text{ Pa}, p_{\infty,g} = 0 \text{ Pa}, \\ q_l &= -5.435 \times 10^5 \text{ J}\cdot\text{kg}^{-1}, q_g = 1,211 \times 10^6 \text{ J}\cdot\text{kg}^{-1}, \\ q'_l &= 0 \text{ J}\cdot\text{kg}^{-1}\cdot\text{K}^{-1}, q'_g = -1054 \times 10^4 \text{ J}\cdot\text{kg}^{-1}\cdot\text{K}^{-1}. \end{aligned}$$

A comparison between SG and Goodwin EOS curves is shown in Fig. 2 for $v_l(T)$, $v_g(T)$, $h_l(T)$, $h_g(T)$, $L_v(T)$. A very good agreement is observed in the considered temperature range for the methanol. The sound speed for vapor and liquid computed by SG method is shown in Fig. 2f.

3.4. Mixture equations of state

The Stiffened Gas EOS for each phase being determined, the aim is now to build the homogeneous mixture EOS. The following definitions and assumptions are used [22]:

– mixture specific volume definition,

$$v = y_g v_g(T_g, p_g) + y_l v_l(T_l, p_l) \quad (20)$$

where $v_k = \frac{1}{\rho_k}$ represent the specific volume of phase k .

– mixture internal energy definition,

$$e = y_g e_g(T_g, p_g) + y_l e_l(T_l, p_l) \quad (21)$$

– mass fraction definition,

$$y_k = \frac{\alpha_k \rho_k}{\rho}, \quad (22)$$

where α_k represent the volume fraction of phase k .

3.5. Thermodynamic closure of the model

The equation of state of system (2) that results from the previous mixture rules and equilibrium constraints $T_g = T_l = T$, $p_g = p_l = p$ reads [28] [22]

$$\begin{aligned} p(\rho, e, y_g) &= \frac{1}{2} [A_g + A_l - (p_{\infty,g} + p_{\infty,l})] \\ &\quad + \sqrt{\frac{1}{4} [A_l - A_g - (p_{\infty,l} - p_{\infty,g})]^2 + A_g A_l} \end{aligned} \quad (23)$$

where

$$\begin{cases} A_k = \left[\frac{y_k(\gamma_k - 1)C_{v,k}}{y_g C_{v,g} + y_l C_{v,l}} \right] [\rho(e - q_k) - p_{\infty,k}] \\ q = y_g q_g + y_l q_l \end{cases} \quad (24)$$

and

$$\begin{cases} y_g = y \\ y_l = 1 - y \end{cases} \quad (25)$$

The mixture temperature is then obtained by

$$\frac{1}{\rho T} = \frac{y_g(\gamma_g - 1)C_{v,g}}{p + p_{\infty,g}} + \frac{y_l(\gamma_l - 1)C_{v,l}}{p + p_{\infty,l}}. \quad (26)$$

3.5.1. Evaporation rate

When phase transition is addressed the last equation of system (2) reads

$$\frac{\partial(\rho y)}{\partial t} + \frac{\partial(\rho y u)}{\partial x} = \rho \frac{y^* - y}{\tau}, \quad (27)$$

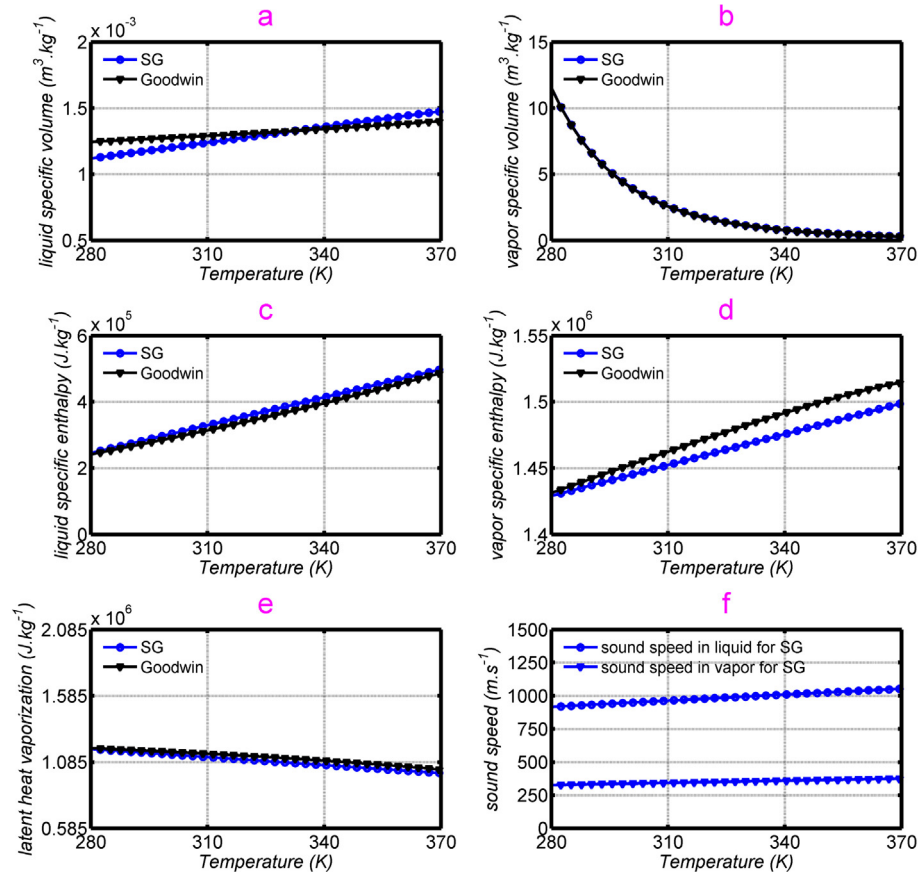


Fig. 2. Comparison of Goodwin and Stiffened Gas equation of state for methanol in the temperature range [280–370 K] on figures a, b, c, d, e and sound speed for vapor and liquid computed by SG method on figure f.

where y^* represents the mass fraction at thermodynamic equilibrium and τ the relaxation time. This time is assumed to tend to zero in the present approach ($\tau \rightarrow 0^+$), where the r.h.s. of Eq. (27), i.e., $\rho \frac{y^* - y}{\tau}$, approaches \dot{m} as y approaches y^* . The assumption of stiff relaxation is consequently free of any parameter and corresponds to local thermodynamic equilibrium [19,20,27]

The mass fraction at equilibrium is computed from the same mixture rules and equilibrium assumptions as before.

When pure phase is present, no thermodynamic equilibrium is assumed. Conversely, if both liquid and vapor phases are present then thermodynamic equilibrium may occur and the condition

$$0 < y < 1 \text{ and } T \geq T_{sat}(p) \quad (28)$$

is satisfied. In this case the liquid and vapor Gibbs free energies are equal;

$$G_g(T_g, p_g) = G_l(T_l, p_l), \quad (29)$$

where G_k denotes the Gibbs free energy of phase k ($G_k = h_k - T_k s_k$).

As $T_g = T_l = T$ and $p_g = p_l = p$, it reduces to

$$G_g(T, p) = G_l(T, p). \quad (30)$$

This equation corresponds to the saturation pressure that also reads

$$p = p_{sat}(T). \quad (31)$$

The mixture mass and mixture energy definition now read

$$\begin{cases} v = y_g v_g(T, p_{sat}(T)) + y_l v_l(T, p_{sat}(T)) \\ e = y_g e_g(T, p_{sat}(T)) + y_l e_l(T, p_{sat}(T)) \\ y_g = 1 - y_l \end{cases} \quad (32)$$

After some simplifications, they become

$$\begin{cases} v = y_g^* v_g(p^*) + y_l^* v_l(p^*) \\ e = y_g^* e_g(p^*) + y_l^* e_l(p^*) \end{cases}, \quad (33)$$

where only two unknowns are present: the mass fraction at equilibrium y^* and the pressure at thermodynamic equilibrium p^* . This non-linear algebraic system is solved following the method given in Le Metayer et al. [28].

The different steps involved in the numerical resolution from one time-step to the other are unfolded in what follows.

1. Assume $\dot{m} = 0$ in Eq. (2d) and compute conservative variables by solving the system of Eqs. (2) (this is a predictor step).
2. Compute the pressure p using Eq. (23).
3. Compute the temperature T using (26).
4. For each cell, test the thermodynamic equilibrium condition (and saturation), Eq. (28) (this is a corrector step).
 - a. If not satisfied, go to next cell (as long as no phase change occurs there and so $\dot{m} = 0$, indeed).
 - b. If satisfied,
 - i. Equilibrium pressure p^* and mass fraction y^* are computed by solving Eq. (33).
 - ii. Set p to p^* and y to y^* .
 - iii. Compute the temperature T using Eq. (31).
5. Go to the next time step.

4. Flow solver

4.1. Godunov type method

The Godunov method consists in partitioning the space domain into computational cells and making space and time integration over each cell of the balance equations. Let us denote

$$\begin{cases} U = (\rho, \rho u, \rho E, \rho y)^T \\ F(U) = (\rho u, \rho u^2 + p, (\rho E + p)u, \rho y u)^T \\ S(U) = (0, -\frac{64\mu}{2D_h^2}u + \epsilon \rho g, \frac{\dot{Q}}{\dot{Q}} + \epsilon \rho g u, \dot{m})^T \end{cases} \quad (34)$$

Hence, Eq. (2) can be written in the following compact form

$$\frac{\partial U}{\partial t} + \frac{\partial F(U)}{\partial x} = S(U). \quad (35)$$

Δt and Δx are time step and cell size respectively, $x_{i-\frac{1}{2}}$ and $x_{i+\frac{1}{2}}$ represent respectively abscissa of the left cell face and the right cell face and $F_{i-\frac{1}{2}}$ and $F_{i+\frac{1}{2}}$ are numerical fluxes calculated at these abscissae. i is the current cell index running from 1 to n , where n is number of cells.

Space integration over the cell $[x_{i-\frac{1}{2}}, x_{i+\frac{1}{2}}]$, see Fig. 3, and a forward time difference scheme approximation of the time derivative term yields the following explicit scheme to be written

$$U_i^{n+1} - U_i^n = \frac{\Delta t}{\Delta x} (F_{i-\frac{1}{2}}^n - F_{i+\frac{1}{2}}^n) + \Delta t S(U_i^n) \quad (36)$$

The Courant–Friedrichs–Lewy (CFL) condition is

$$\Delta t \leq \frac{\Delta x}{\max_i (u_i + c_i)}. \quad (37)$$

In practice, an operator splitting strategy is used to avoid the stiffness due to mass transfer. (See section 4.3 for more details.)

4.2. Harten-Lax-van Leer-Contact Riemann solver

Let us briefly present in this section the numerical method we use to compute fluxes at cell faces. The numerical method is based on HLLC Riemann Solver method, which is an extension made by Toro et al. [29] of the Harten, Lax and van Leer approximate Riemann solver [30] in order to take into account the presence of the contact wave in the Riemann problem solution of Euler equations. Moreover, it is robust and has the property to give always positive fluxes, which is important for the volume fraction and mass fraction variables. This solver is presented in details in the outstanding book of Toro [31].

To compute the HLLC fluxes, the following three steps have to be considered.

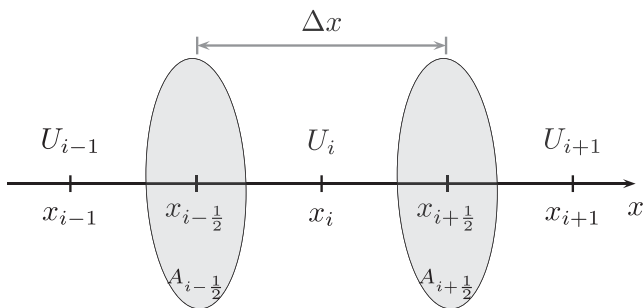


Fig. 3. Sketch of one-dimensional finite volume cells and associated cell faces.

First the right and left facing waves at a given cell boundary separating a left state and a right state, see Fig. 4, are estimated following Davis [32] as

$$S_L = \min\{u_L - c_L, u_R - c_R\} \quad (38)$$

and

$$S_R = \max\{u_L + c_L, u_R + c_R\}, \quad (39)$$

where c is the sound speed.

An intermediate speed S_M is computed by the following relation under Harten-Lax-van Leer (HLL) approximation [30]

$$S_M = \frac{(\rho u^2 + p)_L - (\rho u^2 + p)_R - S_L(\rho u)_L + S_R(\rho u)_R}{(\rho u)_L - (\rho u)_R - S_L \rho_L + S_R \rho_R}. \quad (40)$$

In our case, the mixture sound speed formula suggested by Wood is used [33]

$$\frac{1}{\rho c^2} = \frac{\alpha_l}{\rho_l c_l^2} + \frac{\alpha_g}{\rho_g c_g^2}, \quad (41)$$

where the (pure) phase sound speed is given by

$$c_k = \gamma_k \frac{p + p_{\infty k}}{\rho_k}, \quad k = l, g. \quad (42)$$

Second, U_K^* ($K=L$ for cell left to considered face and $K=R$ for cell right to considered face) is computed by the following relation [34]

$$U_K^* = \rho_K \left(\frac{S_K - u_K}{S_K - S_M} \right) \left[1, S_M, \frac{E_K}{\rho_K} + (S_M - u_K) \left[S_M + \frac{p_K}{\rho_K (S_K - u_K)} \right] \right]^T. \quad (43)$$

Last, the fluxes at the cell faces [29] are computed using the relation

$$F_{i+\frac{1}{2}} = \frac{1}{2} (F_L + F_R) - \text{sign}(S_L) \frac{S_L}{2} (U_L^* - U_L) - \text{sign}(S_M) \frac{S_M}{2} (U_R^* - U_L) - \text{sign}(S_R) \frac{S_R}{2} (U_R - U_R^*). \quad (44)$$

Worth mentioning that in order to take periodic conditions into consideration, the left face flux of the cell $i = 1$ is set equal to the right face flux of cell $i = n$.

4.3. Source terms

Once the Riemann problem is solved, the solution is updated into an intermediate state where the source terms effects are omitted

$$\overline{U}_i^{n+1} = U_i^n + \frac{\Delta t}{\Delta x} (F_{i-\frac{1}{2}}^n - F_{i+\frac{1}{2}}^n) \quad (45)$$

Source terms defined in system (34) are then considered and their contribution is integrated as

$$U_i^{n+1} = \overline{U}_i^{n+1} + \Delta t S(\overline{U}_i^{n+1}) \quad (46)$$

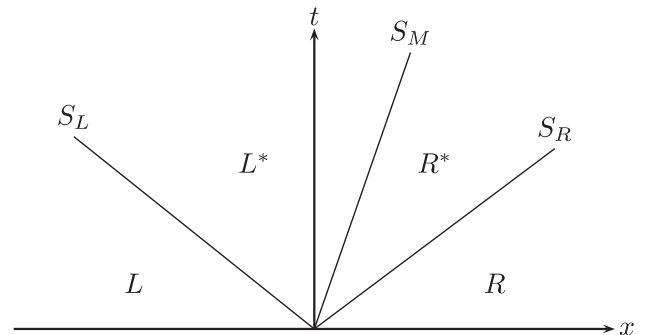


Fig. 4. Representation of Riemann problem under HLLC approximation in the absence of the right hand side in equations of system (2).

This treatment is done for all source terms except the ones expressing mass transfer \dot{m} .

From this, system (33) is solved with state U_i^{n+1} as input. The pressure at thermodynamic equilibrium p^* is thus determined with the help of this non-linear algebraic system and the mass fraction at equilibrium y^* is deduced. The mass fraction y is then reset to the equilibrium value y^* . Doing so, local thermodynamic equilibrium conditions are forced, corresponding to infinitely fast phase transition. Consequently accurate knowledge of parameter τ in (27) and \dot{m} in (34) is useless, as the mass fraction is reset to y^* .

5. Numerical test cases

The aim of this section is to describe and analyze different working cases of 2PLT. For all cases, the loop thermosyphon geometry, the cell size, CFL coefficient, heat exchange coefficient, exchange surface, the temperature of the cold source at the condenser and initial conditions are kept constant. Concerning the geometry, the length of the loop is $L = 1.5$ m and its diameter $D_h = 7$ mm is constant. The horizontal liquid line (A-B), the evaporator (B-C), the vertical vapor line (C-D), the horizontal vapor line (D-E), the condenser (E-F) and the vertical liquid line (F-A) are respectively located between 0 m and 0.25 m, 0.25 m and 0.5 m, 0.5 m and 0.75 m, 0.75 m and 1 m, 1 m and 1.25 m, 1.25 m and 1.5 m. Let us note that a sensitivity to the mesh size analysis of the results was performed (using up to 850 cells) not included here for the sake of brevity. This analysis points up that a 450 cells mesh is needed to get Euclidian error in the velocity profile when steady state is reached less than 7% roughly. So, in the following simulations, the cell size is set to $\Delta x = 3.33 \times 10^{-3}$ m (450 cells for the

whole loop) and the time step Δt deduced from CFL condition (naturally its value depends on the maximum velocity occurring in the loop, but is about 10^{-5} s roughly). We set the temperature of the cold source $T_{cold} = 293.15$ K, the heat exchange coefficient $h_{cond} = 2000 \text{ W} \cdot \text{K}^{-1} \cdot \text{m}^{-2}$ and the exchange surface $A_{ext} = 1.32 \times 10^{-2} \text{ m}^2$, all being assumed constant.

5.1. Initial steady state

The initial steady state is obtained when the power at the evaporator is zero and the loop half-filled with liquid in its lower part. It is computed once and for all. To do so, initial conditions must be given:

$$\begin{aligned}
 p_0 &= 0.13 \times 10^5 \text{ Pa if } x \in [0 \text{ m}, 1.5 \text{ m}], \\
 T_0 &= 293.15 \text{ K if } x \in [0 \text{ m}, 1.5 \text{ m}], \\
 u_0 &= 0 \text{ m} \cdot \text{s}^{-1} \text{ if } x \in [0 \text{ m}, 1.5 \text{ m}], \\
 y_0 &= 0 \text{ and } \rho_0 = 853 \text{ kg} \cdot \text{m}^{-3} \text{ if } x \in [1.25 \text{ m}, 1.5 \text{ m}] \cup [0 \text{ m}, 0.5 \text{ m}] \\
 &\text{(liquid),} \\
 y_0 &= 1 \text{ and } \rho_0 = 10^{-1} \text{ kg} \cdot \text{m}^{-3} \text{ if } x \in [0.5 \text{ m}, 1.25 \text{ m}] \text{ (vapor).}
 \end{aligned}$$

Note that the pressure and the temperature (p_0, T_0) are chosen on the saturation curve initially.

The outputs of the model, without thermal load, such as the density Fig. 5a, the velocity of the mixture Fig. 5b, the internal energy Fig. 5c, the temperature Fig. 5d, the pressure Fig. 5e and the vapor mass fraction Fig. 5f are depicted in Fig. 5. It can be observed that the density, velocity, temperature and vapor mass fraction fields are unaffected. The thermal load at the evaporator being zero, these fields do not change. Nevertheless, the pressure

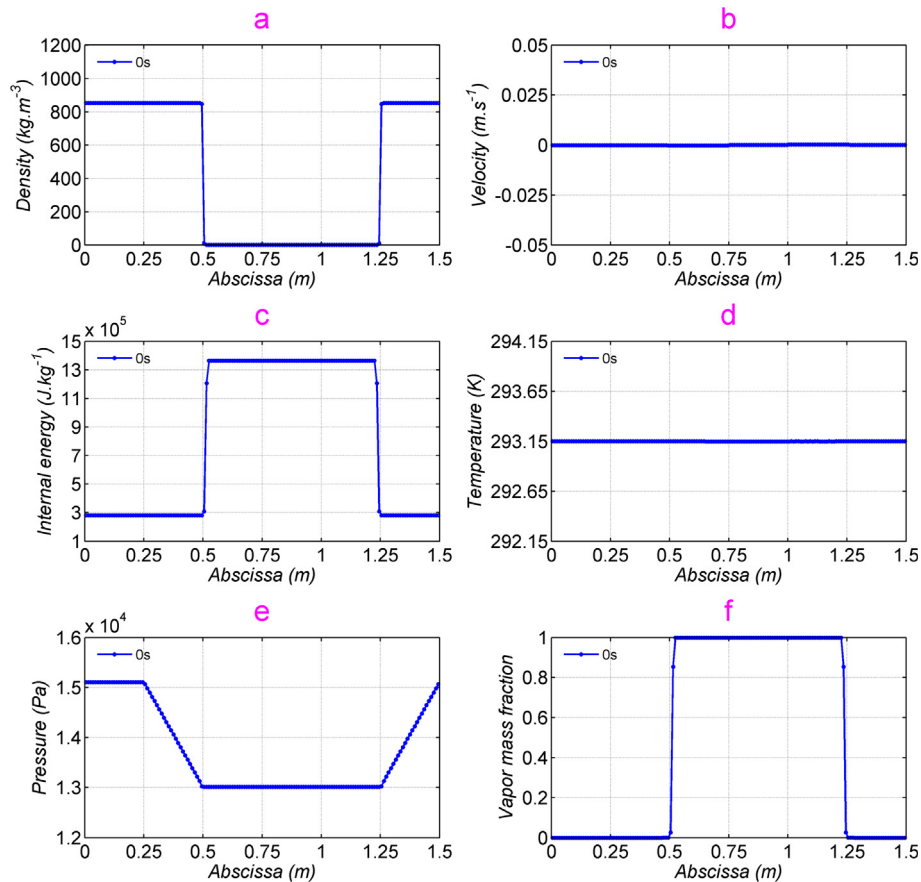


Fig. 5. Initial steady state in thermosyphon loop.

field Fig. 5e is not constant anymore due to the gravity in vertical lines filled with liquid ($\Delta p = \rho g \Delta x$).

Thereafter, 4 test cases of different thermal loads at the evaporator are analyzed and discussed. The thermal load is composed of a ramp whose duration is 5 s and is constant for 45 s afterwards. The final thermal load is set to: 50 W for test case 1, to 250 W for test case 2, to 500 W for test case 3 and to 1000 W for test case 4.

5.2. Test case 1

In this test case, the thermal power at the evaporator after the ramp, is $\dot{Q}_{evap} = 50$ W in steady state ($t = 50$ s). Numerical results are depicted in Figs. 6 and 7. The simulation begins with the initial steady state mentioned above and for $t > 0$, the thermal load evolution at the evaporator and the condenser is shown in Fig. 7. Let us first analyze the evaporator zone (0.25–0.5 m). As expected, applying a nonzero thermal power at the evaporator leads to the internal energy increase. This phenomenon is observed in Fig. 6c between 0.25 m and 0.5 m. The temperature field in Fig. 6d shows weak increase between 0.25 m and 0.4 m in the evaporator. This increase of temperature comes from the liquid heating. Part of thermal load is transferred to sensible heat resulting in liquid temperature rise. The stabilization of the temperature indicates that the fluid is at saturation state. The liquid turns then to vapor by absorbing at the condenser an equivalent latent heat. This behavior is also observed in Fig. 6a and f. Between 0.25 m and 0.4 m in Fig. 6f, the vapor mass fraction goes to zero ($y = 0$). Therefore, the fluid is pure liquid, which is confirmed by Fig. 6a. It can be observed that the density between 0.25 m and 0.4 m decreases weakly. This is due to the dependance of the density with respect to the temperature. Between 0.4 m and 0.5 m in Fig. 6a, density sharply

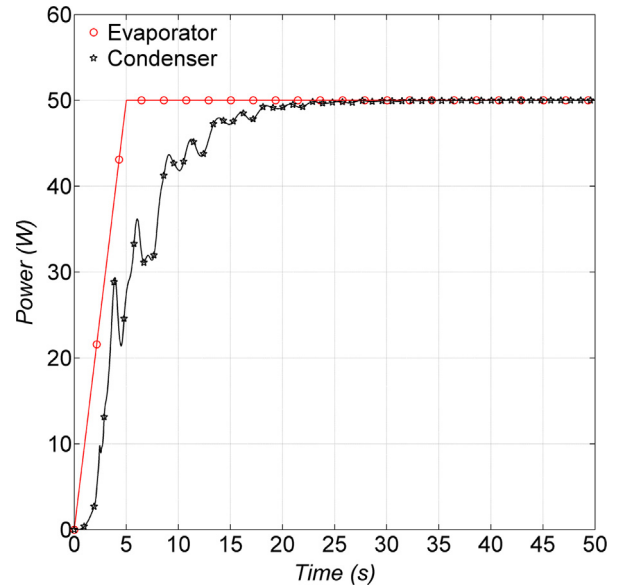


Fig. 7. Time evolution of evaporator and condenser power for $\dot{Q}_{evap} = 50$ W.

decreases, due to the phase-change of methanol. This is confirmed by Fig. 6f where the vapor mass fraction increases. Fig. 6b shows that between 0.25 m and 0.4 m velocity is small ($0.15 \text{ m}\cdot\text{s}^{-1}$) while it increases notably between 0.4 m and 0.5 m. The small velocity between 0.25 m and 0.4 m is due to the presence of liquid in this part. However, when vapor is present, the velocity increases significantly due to both density ratio and mass flow rate conservation.

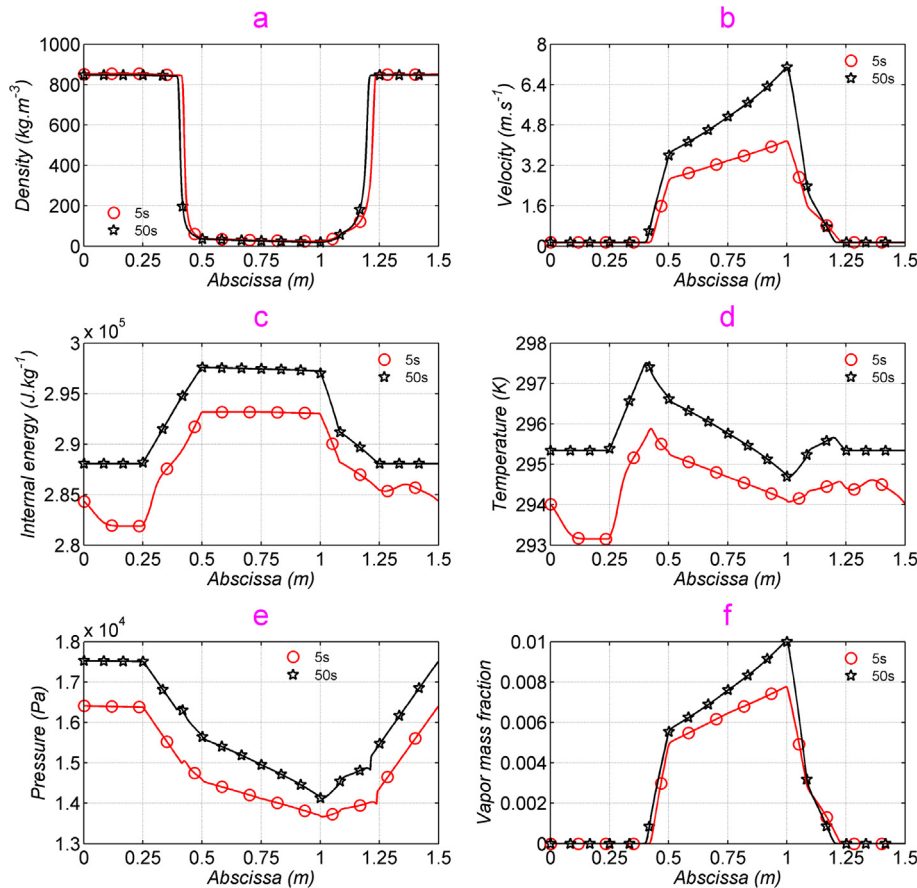


Fig. 6. Space field of flow variables in the thermosyphon loop at 5 s and 50 s for $\dot{Q}_{evap} = 50$ W.

Now let us observe the condenser zone (1–1.25 m). Compared to the evaporator zone, an opposite behavior can be observed in Fig. 6a, b, c, d and f. In fact, heat extraction occurs at the condenser. Hence a large increase of density between 1 m and 1.25 m can be noticed in Fig. 6a. The vapor mass fraction decreases and becomes zero at the outlet of the condenser due to the fact that vapor (Fig. 6f) turns to liquid. The velocity field in Fig. 6b shows that it is greater at the inlet of condenser and decreases widely along the condenser to zero at its outlet. The large velocity at $x = 1$ m is due to the fact that at the condenser inlet, the vapor mass fraction is greater than at the evaporator outlet, which is confirmed observing Fig. 6f where at $x = 1$ m the vapor mass fraction approaches 1%. The large decrease of velocity along the condenser occurs from the phase change along it. At the condenser outlet, there is no more vapor. Hence the fluid is pure liquid which explains the weak velocity at the condenser outlet. Fig. 6c shows a weak decrease of the internal energy, due to heat extraction at the condenser.

Now let us focus on the liquid line (1.25–1.5 m), (0–0.25 m) and the vapor line (0.5–1 m). Fig. 6a, b, c, d, f show roughly constant fields in the liquid line of the loop. This behavior results from the fact that we have supposed these lines adiabatic. Between 1.25 m and 1.5 m in Fig. 6e, the pressure field increases due to the presence of liquid (high density) and gravity but between 0 m and 0.25 m the same figure shows nearly constant field for pressure despite the presence of liquid. This is due to the fact that this part of the loop is horizontal, so gravity is ineffective. In the vapor line (0.5–1 m), Fig. 6b shows that the velocity presents a significant increase in this region. In the same region, observing the pressure field (Fig. 6e) and the density field (Fig. 6a), we notice that pressure and density decrease. The pressure decrease between 0.75 m and

1 m is only due to the viscous effects and between 0.5 m and 0.75 m this drop is due to both viscous and gravity effects. The vapor is compressible and its EOS is perfect gas law. So, neglecting viscous dissipation in the energy balance, the vapor line can be considered adiabatic, in which case the density decreases when the pressure decreases (Fanno flow). This is what is observed in Fig. 6a between 0.5 m and 1 m. In steady state, the mass flow rate ρu is constant along the loop, with a constant area section. This relation leads to an increase of the velocity when the density decreases. This behavior of velocity is observed in Fig. 6b.

The cooling of the fluid about $\Delta T = 3$ K in the vapor line (0.5–1 m) is due to the vapor expansion discussed above. But in the condenser, there is a competition between the fluid compression inducing temperature increase and heat release in the condenser inducing temperature decrease and ultimately subcooling once pure liquid phase is reached, hence a temperature maximum occurs in that region.

Fig. 7 presents the time evolution of thermal power at the evaporator and the condenser. For instance, at 25 s, it can be observed that the thermal load at the condenser is just the opposite the thermal power at the evaporator. This means that the steady state is reached exactly. It worths to note here that the thermal energy transformed into kinetic energy, which allows fluid motion to be maintained, is restored exactly into thermal energy because of dissipation effects, see Eq. (2). Before $t = 25$ s, the heat flux (absolute value) increases globally, with some oscillations. These oscillations are more likely to be physical since their period is of order 1.6 s, quite large for numerical oscillations which the largest period (if any) would be of order $L/|u+c| \approx 1.5/350 = 4$ ms. Moreover, applying the lumped model suggested by Vincent et al. [12] leads to an oscillation period of order $2F\pi\sqrt{\frac{L}{2g}} \approx 1.7$ s (where $\frac{L}{2}$ is

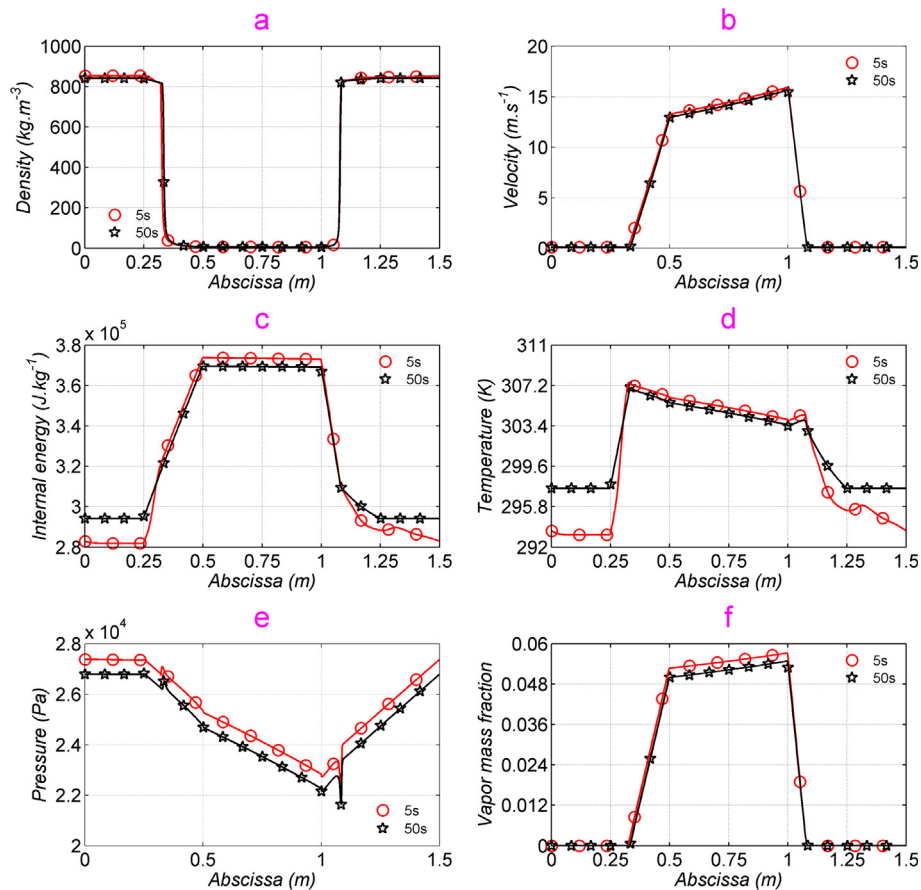


Fig. 8. Space field of flow variables in the thermosyphon loop at 5 s and 50 s for $\dot{Q}_{evap} = 250$ W.

the liquid column length and F a lumped factor of order 1.4), very close to the period experienced here. Worth to mention here that the second-order lumped model suggested by Vincent et al. takes into consideration the exchange between the potential (hydrostatic) and kinetic energies of a moving liquid column in an open U-shaped tube disturbed by some amount of mass (and so height) loss in the evaporator and mass excess in the condenser.

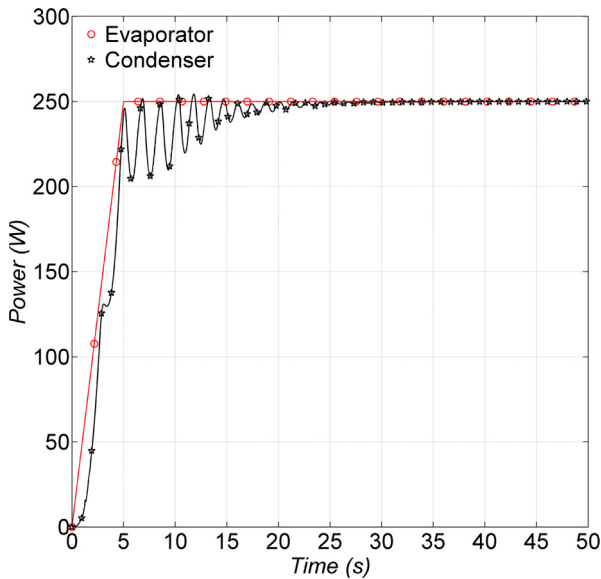


Fig. 9. Time evolution of evaporator and condenser power for $\dot{Q}_{evap} = 250$ W.

5.3. Test case 2

In this case, the thermal power is $\dot{Q}_{evap} = 250$ W at the evaporator. The results are shown in Figs. 8 and 9. The shape of the fields is similar to the test case 1. Nevertheless, the behavior of the loop is emphasized by the increase of thermal load. For instance, let us observe the increase (0.25–0.35 m) and stabilization (0.35–0.50 m) of the temperature in the evaporator in Fig. 8d. Compared with the previous test case, the area of the evaporator, where phase change occurs, is increased due to the higher thermal load. On the same graph in the condenser area, we observe a stabilization around 303 K and then a temperature decrease at the condenser outlet. The fact that the thermal power is higher yields a vapor fraction increasing in the evaporator as shown in Fig. 8f. For the same reason the density at the evaporator outlet is lower in this test case than in test case 1 as depicted in Fig. 8a. The comparison of the graphs b, c, d and e in Figs. 6 and 8 shows that the overall level of velocity, internal energy, temperature and pressure has increased in the present test compared to test 1.

The same vapor expansion, as discussed for the vapor line in test case 1 paragraph, gives rise to equivalent fluid subcooling of the same order of magnitude ($\Delta T = 3$ K) in the vapor line for all heat loads. But the effect of this subcooling is mitigated by the evaporator outlet temperature which is getting higher and higher.

5.4. Test case 3

In this case, the thermal power is $\dot{Q}_{evap} = 500$ W. The time evolution of \dot{Q}_{evap} remains the same as in previous cases. Numerical results are presented in Figs. 10 and 11. The analysis of the fields

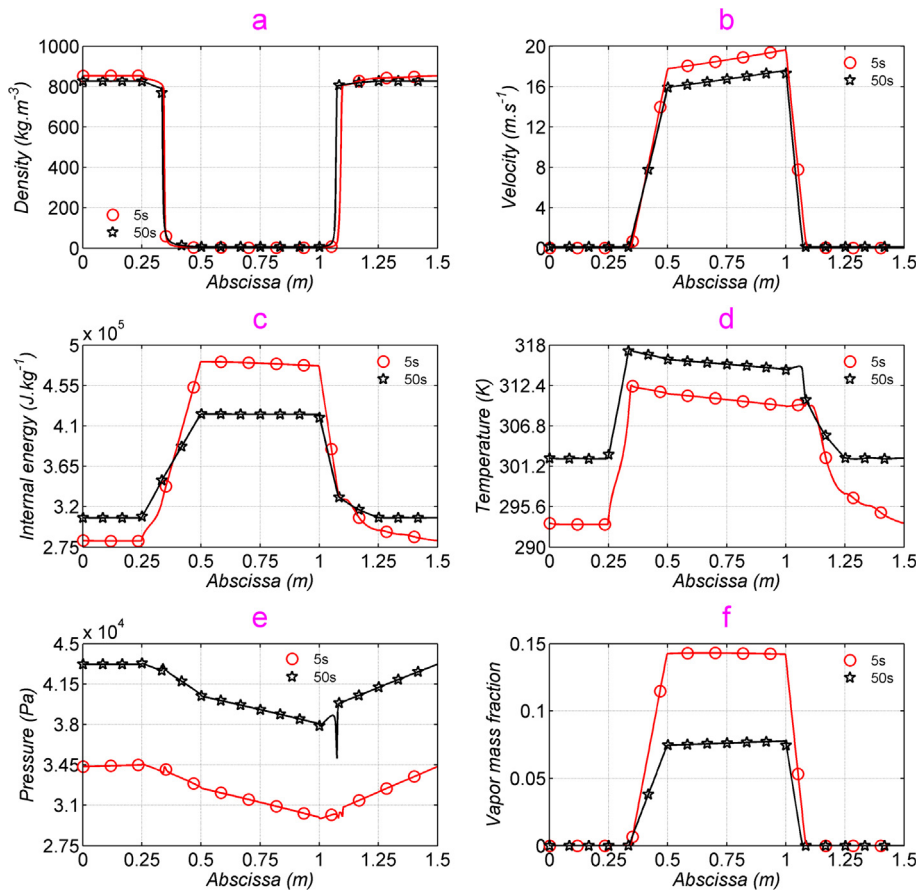


Fig. 10. Space field of flow variables in the thermosyphon loop at 5 s and 50 s for $\dot{Q}_{evap} = 500$ W.

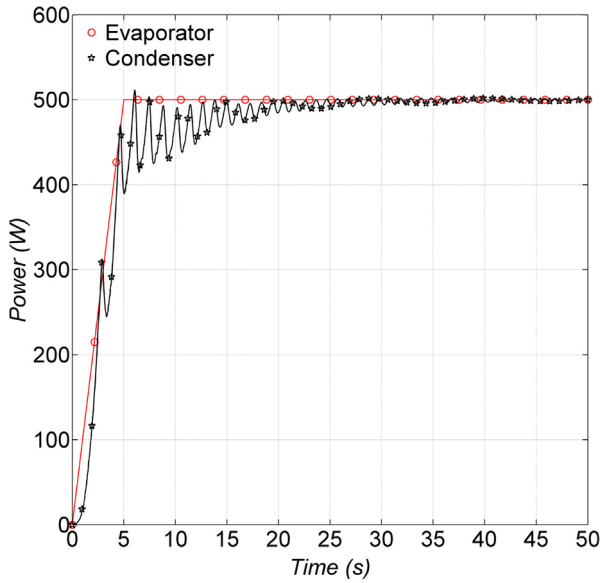


Fig. 11. Time evolution of evaporator and condenser power for $\dot{Q}_{evap} = 500$ W.

is similar to the previous cases. The larger \dot{Q}_{evap} , the larger the space variations of velocity, internal energy and temperature. Note also that the overall pressure level in the loop increases.

In addition, Fig. 10e shows a pressure discontinuity at a position in the condenser where the fluid becomes pure liquid (see Fig. 10f). (The same discontinuity occurs for all thermal powers, see Figs. 6e, 8e and 12e). This discontinuity is a pure numerical effect since

different equations of state are used to describe the mixture and pure phases (and so slightly different speeds of sound may occur when switching between these equations). It is useful to note here that refining the mesh affects both the magnitude and the width of that discontinuity while not changing significantly the pressure profile elsewhere: as a loop is considered, this discontinuity has only a very localized influence.

5.5. Test case 4

For this last test case, $\dot{Q}_{evap} = 1000$ W. Our analyse will focus here on the difference in the space fields at 5s and 50s in Fig. 12. According to Fig. 12d, the saturation temperature at the evaporator outlet ($x = 0.5$ m) is not the same at both times. Now, observing the evolution of thermal power at the evaporator in Fig. 13, we observe at these two times that the thermal power is the same. This means that between 5s and 50s, the system evolves from a saturation state to another saturation state despite the fact that a constant thermal power is applied at the evaporator. This is due to thermodynamic states (p, T, e) of fluid which are not the same at the evaporator input at these times. This is noticeable in Fig. 12c, d, e at position $x = 0.5$ m. This behavior observed at the evaporator inlet and on liquid line (0–0.25 m) is just a consequence of condenser working. In fact, Fig. 13 shows that, at 5s and 50s, the thermal power extracted at condenser is not the same. This is due to the transition from the initial state ($\dot{Q}_{evap} = \dot{Q}_{cond} = 0$ W) to the steady state ($\dot{Q}_{evap} = -\dot{Q}_{cond} = 1000$ W). This also affects the overall level of temperature and pressure in the loop which increases between $t = 5$ s and $t = 50$ s. In Fig. 12f at the outlet of the evaporator at position ($x = 0.5$ m), it can be noticed that the vapor fraction

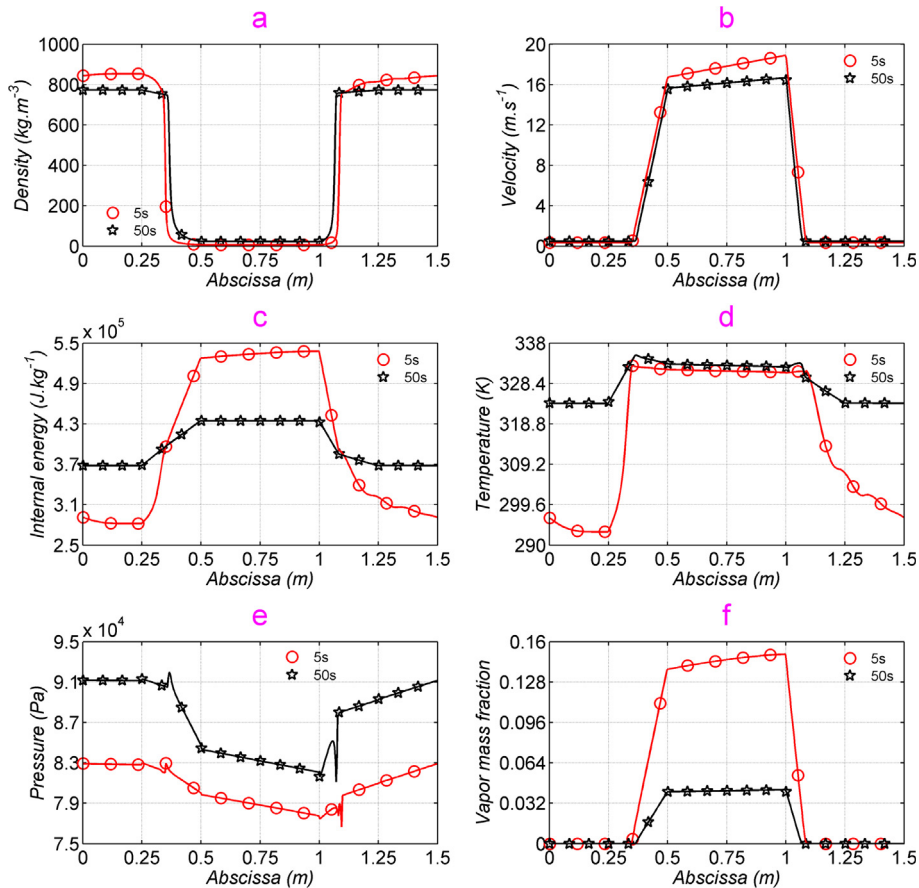


Fig. 12. Space field of flow variables in the thermosyphon loop at 5s and 50s for $\dot{Q}_{evap} = 1000$ W.

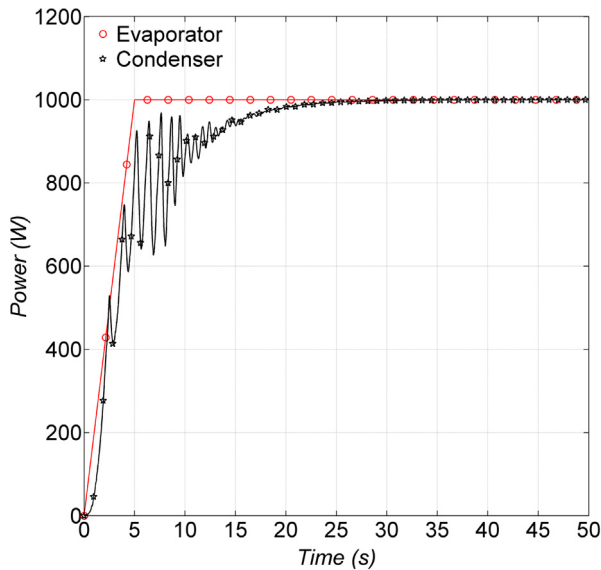


Fig. 13. Time evolution of evaporator and condenser power for $\dot{Q}_{evap} = 1000$ W.

decreases between 5 s and 50 s. This is confirmed by Fig. 12a at the same position. The low duration of the ramp of \dot{Q}_{evap} explains these observations. When the ramp duration is small, the fluid is heated in a short time. So a large increase of internal energy visible in Fig. 12c, is observed and so a quick creation of vapor. The immediate consequence is that the flow at the evaporator outlet stores more energy at 5 s than at 50 s. This means that the velocity at the outlet of the evaporator at 5 s is greater than at 50 s, which is confirmed by Fig. 12b. The density field at 5 s is greater than at 50 s between 0 m and 0.35 m and between 1.1 m and 1.5 m. But observing Fig. 12d, we notice an opposite behavior of the temperature field. This means that on this area, the fluid is warmer at $t = 50$ s than at $t = 5$ s, consequently, the density at 50 s is lower than at 5 s.

Note that the fact that the saturation temperature at 5 or 50 s is different did already happen in all cases, though the highest power load exacerbates that difference. The same applies for the inlet temperature of the evaporator. And all this behavior is a consequence of the pressure increase that comes from the condenser power dependence upon the time-varying local fluid temperature. This behavior is not a particular feature of case 4, but is a general trend of this kind of closed self-pressurized loop thermosyphon.

In should be mentioned that the two-phase length inside the evaporator decreases between 250 and 1000 W, in opposite to what occurs between 50 and 250 W.

6. Conclusion

In this paper, a 2PLT model is build. The closed-form of the thermodynamic state laws of methanol have been approximated by the SG EOS. The numerical resolution is carried out using a finite volume approach with a one-dimensional space discretization of the loop and a HLLC Riemann solver. The various test cases show that the overall levels of density, pressure, velocity, temperature, internal energy and vapor mass fraction in the loop change considerably when the power load at the evaporator increases. The numerical results of all test cases show that the model reproduces satisfactorily the behavior of a classical loop and reveals the different mechanisms of energy storage in its different forms when thermal load is applied.

References

- [1] E.L. Long, The long thermopile, in: Proceedings Permafrost International Conference, 1963, pp. 487–491.
- [2] C. Sarno, C. Tantolin, R. Hodot, Y. Maydanik, S. Vershinin, Loop thermosyphon thermal management of the avionics of an in-flight entertainment system, *Appl. Therm. Eng.* 51 (2013) 764–769.
- [3] A. Samba, H. Louahlija-Gualous, S.L. Masson, D. Nörterhäuser, Two-phase thermosyphon loop for cooling outdoor telecommunication equipments, *Appl. Therm. Eng.* 50 (2013) 1351–1360.
- [4] J. Li, F. Lin, G. Niu, An insert-type two-phase closed loop thermosyphon for split-type solar water heaters, *Appl. Therm. Eng.* 70 (2014) 441–450.
- [5] C.C. Chien, C.K. Kung, C.C. Chang, W.S. Lee, C.S. Jwo, S.L. Chen, Theoretical and experimental investigations of a two-phase thermosyphon solar water heater, *Energy* 36 (2011) 415–423.
- [6] B.S. Larkin, An experimental study of the two-phase thermosyphon tube, *Trans. Canadian Soc. Mech. Eng.* 14 (B-6) (1971) 1–8.
- [7] P. Zanocco, M. Giménez, D. Delmastro, Modeling aspects in linear stability analysis of a self-pressurized, natural circulation integral reactor, *Nucl. Eng. Des.* 231 (2004) 283–302.
- [8] C. Marcel, H. Furci, D. Delmastro, V. Masson, Phenomenology involved in self-pressurized, natural circulation, low thermodynamic quality, nuclear reactors: the thermal-hydraulics of the carem-25 reactor, *Nucl. Eng. Des.* 254 (2013) 218–227.
- [9] C. Marcel, F. Acuña, D. Delmastro, V. Masson, Stability of self-pressurized, natural circulation, low thermo-dynamic quality, nuclear reactors: the stability performance of the carem-25 reactor, *Nucl. Eng. Des.* 265 (2013) 232–243.
- [10] H.H. Bau, K.E. Torrance, On the effects of viscous dissipation and pressure work in free convection loops, *Int. J. Heat Mass Transfer* 26 (1983) 727–734.
- [11] D.B. Kreitlow, G.M. Reistad, C.R. Miles, G.G. Culver, Thermosyphon models for downhole heat exchanger applications in shallow geothermal systems, *J. Heat Transfer* 100 (1978) 713–719.
- [12] C.C.J. Vincent, J.B.W. Kok, Investigation of the overall transient performance of the industrial two-phase closed loop thermosyphon, *Int. J. Heat Mass Transfer* 35 (1992) 1419–1426.
- [13] W. Leidenfrost, P. Modrei, Flow conditions and heat transfer in a two-phase closed loop thermosyphon, *ASME Fluids Eng. Div.* 61 (1987) 185–192.
- [14] F. Dobran, Steady-state characteristics and stability thresholds of a closed two-phase thermosyphon, *Int. J. Heat Mass Transfer* 28 (5) (1985) 949–957.
- [15] J.G. Reed, C.L. Tien, Modelling of two phase closed thermosyphon, *J. Heat Transfer* 10913 (1987) 722–730.
- [16] N.Z. Aung, S. Li, Numerical investigation on effect of riser diameter and inclination on system parameters in a two-phase closed loop thermosyphon solar water heater, *Energy Convers. Manage.* 75 (2013) 25–35.
- [17] T. Yilmaz, Computer simulation of two-phase flow thermosyphon solar water heating system, *Energy Convers. Manage.* (1991) 33–144.
- [18] H. Bielinski, J. Mikielewicz, Natural circulation in single and two phase thermosyphon loop with conventional tubes and minichannels, *Heat Transfer-Math. Model. Numer. Methods Inform. Technol.* 19 (2011) 474–496.
- [19] W. Qu, Hydrodynamics of two-phase loop thermosyphon, *Front. Heat Pipes* 1 (2010) 1–7.
- [20] E. Ramos, M. Sen, C. Trevino, A steady-state analysis for variable area one-and two-phase thermosyphon loops, *Int. J. Heat Transfer* 28 (9) (1985) 1711–1719.
- [21] R. Saurel, P. Boivin, O. Le Metayer, A general formulation for cavitating, boiling and evaporating flows, *Comput. Fluids* (2016) 1–45.
- [22] S. Le Martelot, R. Saurel, O. Le Metayer, Steady one-dimensional nozzle flow solutions of liquid-gas mixtures, *J. Fluid Mech.* 737 (2013) 146–175.
- [23] R. Saurel, F. Petitpas, R. Abgrall, Modelling phase transition in metastable liquids: application to cavitating and flashing flows, *J. Fluid Mech.* 607 (2008) 313–350.
- [24] A. Cicchitti, C. Lombardi, M. Silvestri, G. Soldaini, R. Zavattarelli, Two-phase cooling experiments: pressure drop, heat transfer and burnout measurements, *Energia Nucl.* 7 (6) (1960) 407–425.
- [25] N. Blet, Analyse expérimentale et par voie de modélisation d'une boucle gravitaire à pompage capillaire multi-évaporateurs, Ph.D. thesis, 2014.
- [26] R.D. Goodwin, Methanol thermodynamic properties from 176 to 673 k at pressures to 700 bar, *J. Phys. Chem. Ref. Data* 16 (1987) 888–896.
- [27] O. Le Metayer, J. Massoni, R. Saurel, Elaborating equations of state of a liquid and its vapor for two-phase flow models, *J. Therm. Sci.* 24 (2004) 265–276.
- [28] O. Le Metayer, J. Massoni, R. Saurel, Dynamic relaxation processes in compressible multiphase flows: application to evaporation phenomena, *ESAIM: PROC.* 40 (2013) 103–123.
- [29] E. Toro, M. Spruces, W. Speares, Restoration of the contact surface in the HLL Riemann solver, *Shock Waves* 4 (1) (1994).
- [30] A. Harten, P. Lax, B. van Leer, On upstream differencing and Godunov-type schemes for hyperbolic conservation laws, *SIAM Rev.* 25 (1) (1983) 35–61.
- [31] E. Toro, *Riemann Solvers and Numerical Methods for Fluid Dynamics: A Practical Introduction*, vol. 4(1), Springer Science and Business Media, 2013.
- [32] S. Davis, Simplified second-order godunov-type method, *SIAM J. Sci. Stat. Comput.* 9 (3) (1988) 445–473.
- [33] Wood, *A Textbook of Sound*, vol. 19, Bell Eds, 1930.
- [34] E.F. Toro, *Riemann Solvers and Numerical Methods for Fluid Dynamics*, vols. 1–12, Springer, 2009.